Materials Horizons

Visualizing Defect Energetics

Journal:	*Materials Horizons*
Manuscript ID	MH-COM-03-2021-000397.R1
Article Type:	Communication
Date Submitted by the Author:	09-May-2021
Complete List of Authors:	Anand, Shashwat; Northwestern University, Materials Science and Engineering Male, James; Northwestern University, Materials Science and Engineering Wolverton, Chris; Northwestern University, Department of Materials Science and Engineering Snyder, G.; Northwestern University, Materials Science

New Concepts

The study of point defects is relevant to practically all materials science applications. The defect formation energy ΔH_{def} is an important property which relates to off-stoichiometry, electronic dopability and ionic conductivity of the material. The value ΔH_{def}, which expresses the stability of the defect in the compound, depends on the chemical conditions under which the material is synthesized. Currently, describing this chemical control of defects first requires plotting the phase stability of the compound separately in chemical potential space where, in comparison to the composition space, the visualization is relatively abstract. Stability visualization of compounds in composition space, represented by formation Enthalpy (ΔH_{form}) versus composition convex-hull plots, are already widely understood and used by the materials science community in first-principles based high-throughput databases and phase diagram assessments. In this work we show that ΔH_{def} of point defects can also be visualized within a 2-dimensional convex-hull construction *regardless* of the number of components in the system and choice of chemical condition. This conceptual insight integrates stability visualization of point defects with that of the compound and will help to build an intuition for defect engineering among a wider materials science audience which internalizes the simple concept of convex-hulls in introductory courses.

Visualizing Defect Energtics

Shashwat Anand*, James P. Male, Chris Wolverton, and G. Jeffrey Snyder*

Department of Materials Science and Engineering, Northwestern University, Evanston

E-mail: sanand@lbl.gov

Abstract

Defect energetics impact most thermal, electrical and ionic transport phenomena in crystalline compounds. The key to chemically controlling these properties through defect engineering is understanding the stability of (a) the defect and (b) the compound itself relative to competing phases at other compositions in the system. The stability of a compound is already widely understood in the community using intuitive diagrams of formation enthalpy (ΔH_f) vs. composition, in which the stable phases form the 'convex-hull'. In this work, we re-write the expression of defect formation enthalpy (ΔH_{def}) in terms of the ΔH_f of the compound and its defective structure. We show that ΔH_{def} for a point defect can be simply visualized as intercepts in a two-dimensional convex-hull plot *regardless* of the number of components in the system and choice of chemical conditions. By plotting ΔH_f of the compound and its defects all together, this visualization scheme directly links defect energetics to the compositional phase stability of the compound. Hence, we simplify application level defect thermodynamics within a widely used visual tool understandable from basic materials science knowledge. Our work will be beneficial to a wide community of experimental chemists seeking to build an intuition for appropriate choice of chemical conditions for defect engineering.

Introduction

Introductory textbooks in materials science often tabulate values of defect formation enthalpy (ΔH_{def}) of intrinsic defects in crystalline solids. These tables typically compare ΔH_{def} for intrinsic defects in elemental metals, such as Ti, Co, Ni, W, etc. Other common examples involve comparisons of intrinsic Schottky and Frenkel defects in ionic compounds such as NaCl, KCl, AgCl, CaF_2, etc. In each of these cases, the defect does not alter the overall composition of the structure, and stability of the defect is determined with respect to the pristine host structure. Hence, ΔH_{def} for all such defect types takes a single value at given temperature and pressure allowing for a simple comparison and understanding of defects.

In contrast, the defect energetics of most other important point defects in crystalline compounds such as interstitials, vacancies and anti-sites is significantly more complicated. For compounds, with two or more elements, even these simple defects, will alter the overall composition. Hence, the stability of the defect must be assessed with respect to stable phases lying at other compositions in the system, instead of just the pristine host structure of the compound. For example, when NaCl is saturated with a Cl atmosphere, the stability of a Na-vacancy defect is determined with respect to NaCl and Cl_2 gas. When NaCl is saturated with elemental Na on the other hand, stability of the same defect is determined NaCl and metallic Na. As a result, unlike a Schottky defect in NaCl, the stability of the Na-vacancy defect can vary depending on the chemical equilibrium conditions and $\Delta H_{\text{Na-vacancy}}$ will take one value corresponding to Na-saturated conditions and another corresponding to Cl-saturated conditions. Hence, ΔH_{def} of simple point defects in crystalline compounds can take at least two values of defect energies which are 'chemically controllable'.

The dependence of defect energetics on phase equilibrium allows for chemical control of any properties that are affected by point defects. In semiconductor compounds, for example, intrinsic charged defects set a thermodynamic limit on the number of charge carriers, or dopability,[1,2] in the system. Changing chemical equilibrium conditions to tune ΔH_{def} of intrinsic defects can offset this limit to allow more carriers in the semiconductor, thereby

opening a wider range of electronic properties. For instance, in state-of-the-art n-type thermoelectrics PbTe and Mg_3Sb_2, electron dopability is barely possible unless the compounds are synthesized under cation-rich chemical conditions.[3,4] Point defects also impact electrical,[5,6] thermal[7,8] and ionic[9–13] transport significantly, making them important in studies for a variety of applications such as batteries,[14–16] photovoltaics,[17,18] thermoelectrics,[19–22] thermochemical water splitting,[23,24] solid oxide fuel cells,[25,26] and transparent conducting oxides.[27] In view of the fact that practically all materials research focuses on properties impacted by simple defects in some way, understanding defect energetics within a thermodynamic framework which is widely used by the community will be very beneficial.

Formation enthalpies (ΔH_f) are the most commonly used thermochemical quantity for composition dependent stability analysis. Given the ΔH_f for all possible phases in a system, plotting them in composition space is sufficient to distinguish the stable phases from the unstable ones. These plots, also known as convex-hulls, are commonly used to introduce the subject of thermodynamic stability through the common tangent construction. As a result, convex-hulls are widely used by the scientific community for reading stability prediction of compounds presented in high-throughput databases such as OQMD,[28,29] Materials Project,[30] AFLOW library,[31] and performing stability analysis using CALPHAD assesments.[32,33]

In this work, we demonstrate that one can graphically solve for ΔH_{def} of simple point defects within the convex-hull construction itself (see Figure 1). The ΔH_{def} of a defect involving the atom A (A-vacancy and A-interstitial), for example, can be simply visualized as intercepts on the elemental A axis of the convex-hull diagram (see Figure 1). Since these elemental axes in the convex-hull diagrams represent the atomic chemical potential scale, one can visualize ΔH_{def} *regardless* of the chemical conditions considered. Hence, our visualization scheme takes into account the stability of both the defect as well as the compound in ΔH_{def} calculation. Furthermore, we also show that the graphical solution of ΔH_{def} for any complex multicomponent (ternaries, quaternaries etc.) compound can be visualized in simple two-dimensional plots without any loss of information. Since our approach simplifies

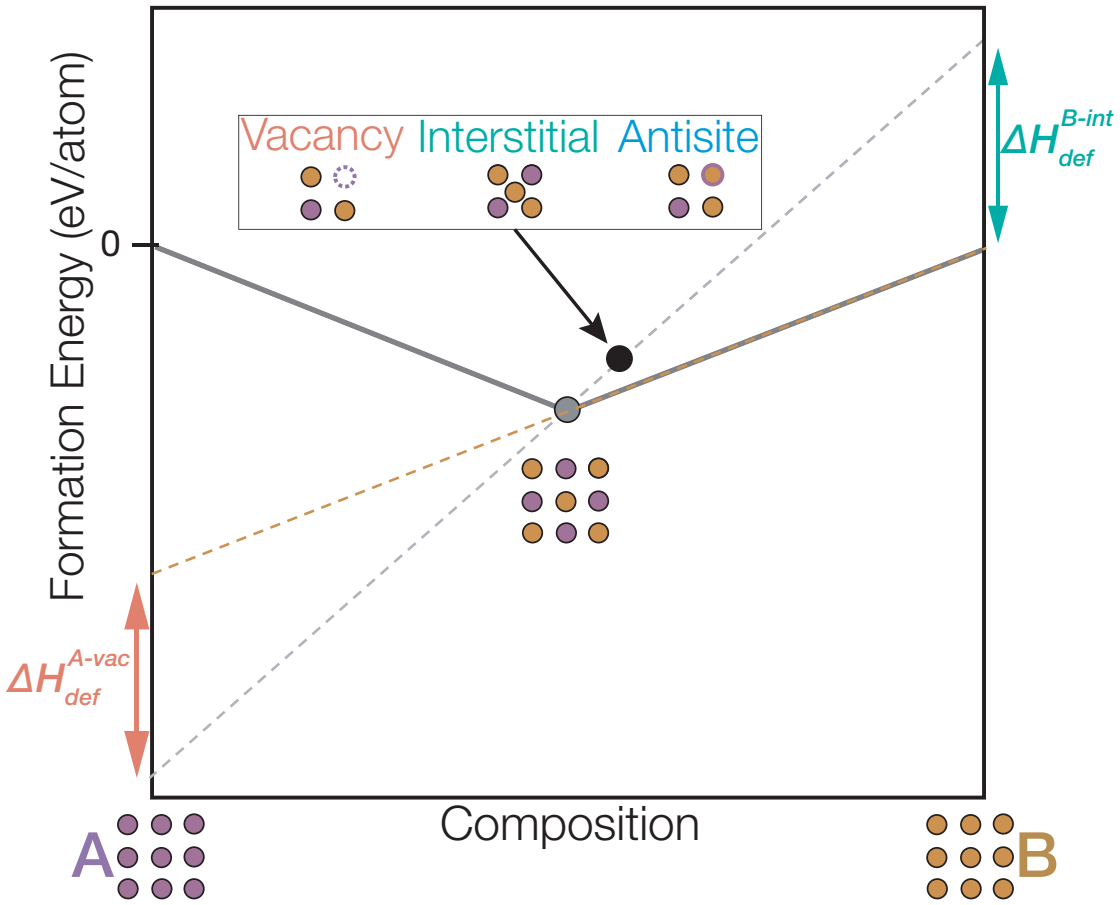

Figure 1: Sketch showing the graphical solution for defect formation enthalpy for defects (black circle) in the compound AB (grey circle) for B-rich equilibrium conditions (ends of the orange dashed line represents the atomic chemical potentials). The compound AB is the only stable phase in the $A-B$ convex-hull (thick grey lines). The defective structure (black circle) could represent any one of three defects: (i) A-vacancy, (ii) B-interstitial or (iii) B_A anti-sites. The defective structure lies above the convex hull, indicating positive ΔH_{def}. The graphical solution for ΔH_{def} (i) (ΔH_{def}^{vac}) and (ii) (ΔH_{def}^{int}) can be visualized as intercepts on the A and B axis respectively.

application level defect thermodynamics using basic materials thermodynamics knowledge, we expect it to be a useful pedagogical tool for a wide community.

We begin by introducing the concept of convex-hulls for finite-temperature and $T = 0$ K phase stability analysis. We follow this with a discussion of defect formation energies. Finally, we will describe our visualization scheme for ΔH_{def} of model binary and ternary compounds within the two-dimensional $T = 0K$ convex-hull framework.

Results and Discussion

Finite Temperature

At non-zero temperatures, thermal energy (kT) creates defects in the lattice of a compound and changes its composition. The off-stoichiometry observed with increasing temperature can be visualized in a temperature-composition phase diagram. Figure 2a sketches the composition-temperature phase diagram of a model binary ($A-B$) system for which the phases A, B, and AB, (depicted by shaded regions) all exhibit single phase width and are stable in the entire temperature range. In general, the maximum amount of off-stoichiometry in the stable single phase regions increases with temperature due to larger amounts of thermal energies available to form defects in the lattice. The white regions bordered by single phases represent two-phase equilibrium.

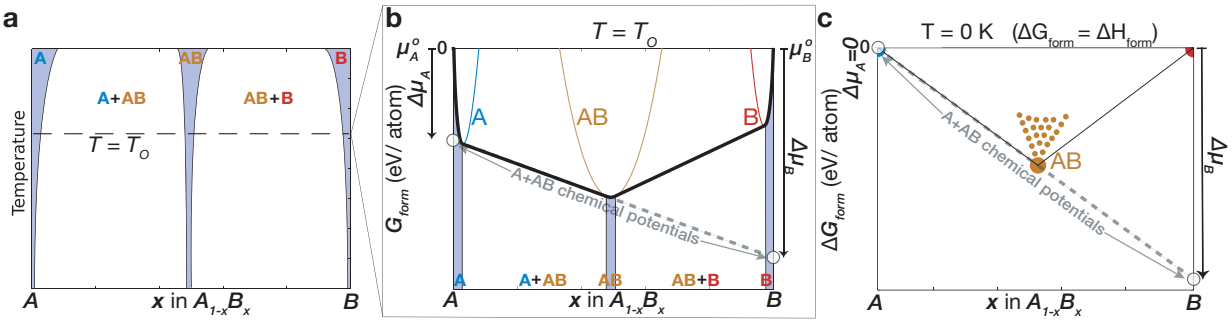

Figure 2: (a) Temperature-Composition phase diagram for a model binary system $A-B$ with three solid phases A, B and AB, and their adjoining two-phase regions. (b) Example free energy (ΔG_f) models of the phases A (blue curve), B (red curve), AB (orange curve) at the temperature $T=T_0$ in panel (a). Thick black lines drawn at the common tangents between the stable phases represent the lowest energy surface and determine compositional limits of the phase boundaries. (c) At 0 K, the Gibbs curves in (b) collapse and ΔG_f for each compound becomes a point (ΔH_f). Common tangents drawn between stable phases form the 0 K low energy surface, or convex-hull.

Solubility of different elements (at $T=T_o$, for example, see Figure 2a) within each phase can be simply understood using the Gibbs free energies of formation (ΔG_f) of all stable phases (see Figure 2b). ΔG_f can be drawn as composition-dependent curves for each phase, where ΔG_f at a particular composition is determined with respect to the free energy of

elemental phases A (G_A^0) and B (G_B^0). For example, the free energy of formation for the compound AB_2, for example, at the composition $x = 2/3$ is given by

$$\Delta G_f^{AB_2} = G_{AB_2} - 1/3 \times G_A^0 - 2/3 \times G_B^0 \quad (1)$$

where G_{AB_2} is the free energy of the AB_2 compound in eV/ atom. It is important to note that when calculated on a per-atom basis (as in Figure 2 b) G_A^0 and G_B^0 are actually the *elemental* chemical potentials (μ_A^0 and μ_B^0) at constant pressure. Hence, the formation energy are all relative to the elemental chemical potentials and ΔG_f at the percentage composition $x = 0$ and $x = 1$ is zero (see Figure 2b).

The stability of a phase or combination of phases as seen in the phase diagram (see $T = T_0$ in Figure 2a) is determined by the common tangent construction; a topic familiar from introductory texts on phase diagrams. In this technique, common tangents connecting the ΔG_f curves of all the phases involved are drawn and the lowest free energy surface (see thick lines in Figure 2b) is chosen in order to describe phase stability. This lowest energy surface, consisting of linear and non-linear (see thick black lines in Figure 2b) portions is known as the *convex-hull* of the $A - B$ system. The linear portions drawn from connecting common tangents between curves indicate compositions which undergo phase separation in order to lower the system's energy to that of the common tangent line. The non-linear portion of the convex-hull is created by a single low energy ΔG_f curve and indicates a single phase region. ΔG_f curves for metastable phases which cannot be seen in the phase diagram can also be represented by curves lying above the convex-hull.

In addition to demonstrating compositional stability, convex-hull constructions also contain complete information on how the chemical potentials of A and B atoms vary across the entire composition range. To obtain the chemical potentials of the elements A and B at a particular composition, one can simply draw a tangent to the convex-hull at that composition and extend it in either direction to find the intercepts on the A ($x = 0$) and B-component ($x = 1$) y-axis. The intercept length along the y-axis (given in eV/atom)

indicates change in chemical potentials with respect to that of the elemental species μ_A^0 (for A) and μ_B^0 (for B), respectively. So the chemical potentials for the A-AB equilibrium in Figure 2b, for example, is $\mu_A^0 + \Delta\mu_A$ and $\mu_B^0 + \Delta\mu_B$ (see dashed grey line). The constant values of the chemical potential across the two phase composition range signifies the energy gain/loss associated with exchanging a single atom between phases in equilibrium (A and AB for example). We discuss plotting chemical potential diagrams using the convex-hull construction in Supplementary information.

T = 0 K

The curvature in the finite temperature ΔG_f arises from the entropic contribution ($-T\Delta S$) to the free energy, which typically varies non-linearly with composition. So at $T = 0K$, where $\Delta G_f = \Delta H_f$, the curvature associated with the entropic contribution vanishes for all phases, and the stable phases are represented by single points (see large circles in Figure 2c) lying on the convex-hull. These points indicate ΔH_f of the defect-free stoichiometric structure of the compound. The composition dependence of ΔH_f at $T = 0K$ for the stable phases is be depicted by including the energies of its defective structures in the convex-hull diagram. The composition of these defective structures deviate from the nominal stoichiometry of the compound in case of point defects such as vacancies, interstitials and anti-site defect. So structures with larger concentrations of point defects in the compound AB, for example, will lie further away from it in composition. The ΔH_f of these defective structures (see small orange points for AB phase in Figure 2c) lie above the convex-hull signifying that they are metastable at $T = 0K$.

Defect Energy

Consider, for example, the following defect reaction involving formation of an A-vacancy from the bulk of a model binary compound AB

$$AB \rightarrow A_{1-\delta}B + \delta\, A \tag{2}$$

the composition of the AB phase changes slightly (δ) and the atom removed from AB gets placed in the elemental phase A. The molar enthalpy for such a defect reaction (ΔH_D) is given by

$$\Delta H_D = H(A_{1-\delta}B) + \delta\, H(A) - H(AB) \tag{3}$$

where $H(A)$, $H(AB)$ and $H(A_{1-\delta}B)$ are the molar enthalpies of A, AB and the defective structure. It is important to note that in addition to the enthalpy associated with the host structure $[H(AB)]$ and defect structure $[H(A_{1-\delta}B)]$, the defect formation enthalpy ΔH_D also depends on the enthalpy of the phase where the atom ends up $[H(A)]$. So ΔH_D in AB could in principle be evaluated for any combination of phases (AB-A, AB-AB_3, etc.). However, ΔH_D is well-defined only if the phases are in thermodynamic equilibrium; i.e. the phases involved constantly exchange atoms with each other without spontaneously forming reaction product phases. The phase AB can be in equilibrium with a relatively A-poor phase (i.e. AB_3, B) and a relatively A-rich phase (i.e. A_3B, A) in the $A-B$ binary system. So depending on which equilibrium AB is participating in, $H(A)$ in equation 3 can be substituted by the enthalpy of another phase in the binary system. Consequently, ΔH_D can take different values based on the choice of chemical equilibrium conditions. The multiple values of ΔH_D is in stark contrast to intrinsic defects in elemental solids or even Schottkey and Frenkel defects in ionic solids (see Methods section). Even the simple binary compounds can participate in more than two equilibria if a multicomponent composition space (ternary (for example Na doping in PbTe), quaternary, pentenary etc.) is considered, making the problem significantly more complicated.

Since the defect formation enthalpy is defined on a per-defect basis in the dilute limit where $\lim \delta \rightarrow 0$, we re-write the equation 3 for a single vacancy defect (ΔH_{def}) by replacing

$H(A)$ with the chemical potential of the atom A (μ_A) and write it as

$$\Delta H_{def} = E_{defect} - E_{pristine} + \mu_A \quad (4)$$

where the first term E_{defect} - $E_{pristine}$ is the difference in energy between the defective and pristine (defect-free) structures. More generally, ΔH_{def} for all types of point defects (interstitials, vacancies and antisites) can be written as:

$$\Delta H_{def} = E_{defect} - E_{pristine} - \Sigma\, \Delta N_i \mu_i \quad (5)$$

where ΔN_i is the number of atoms of species i added to or removed from the defective structure (+1 for interstitials, -1 for vacancies and for antisites +1 and -1 for the atomic species added and the atom species missing respectively) and μ_i is the chemical potential of the species i.

ΔH_{def} of charged defects, can also have an additional dependence on the position of the equilibrium Fermi-level (E_F) itself[34] which can be expressed as

$$\Delta H_{def} = E_{defect} - E_{pristine} - \Sigma\, \Delta N_i \mu_i + qE_F \quad (6)$$

where q is the charge state of the defect. For a fixed value of E_F, the dependency of the charged defect ΔH_{def} on chemical conditions — described by the $\Sigma\, \Delta N_i \mu_i$ term — is the same as that of a charge neutral defects (see Equation 5). In the following sections we describe the visualization scheme for ΔH_{def} of charge neutral and charged point defects (at a fixed E_F).

Graphical representation of point defect energies in convex-hulls

To visualize the defect formation energy, ΔH_{def} , within the convex hull construction (see Figure 3), we re-write equation 5 in terms of the formation energies ΔH_f of the defective and pristine structures and simplify the expression (see Methods section). In this new form

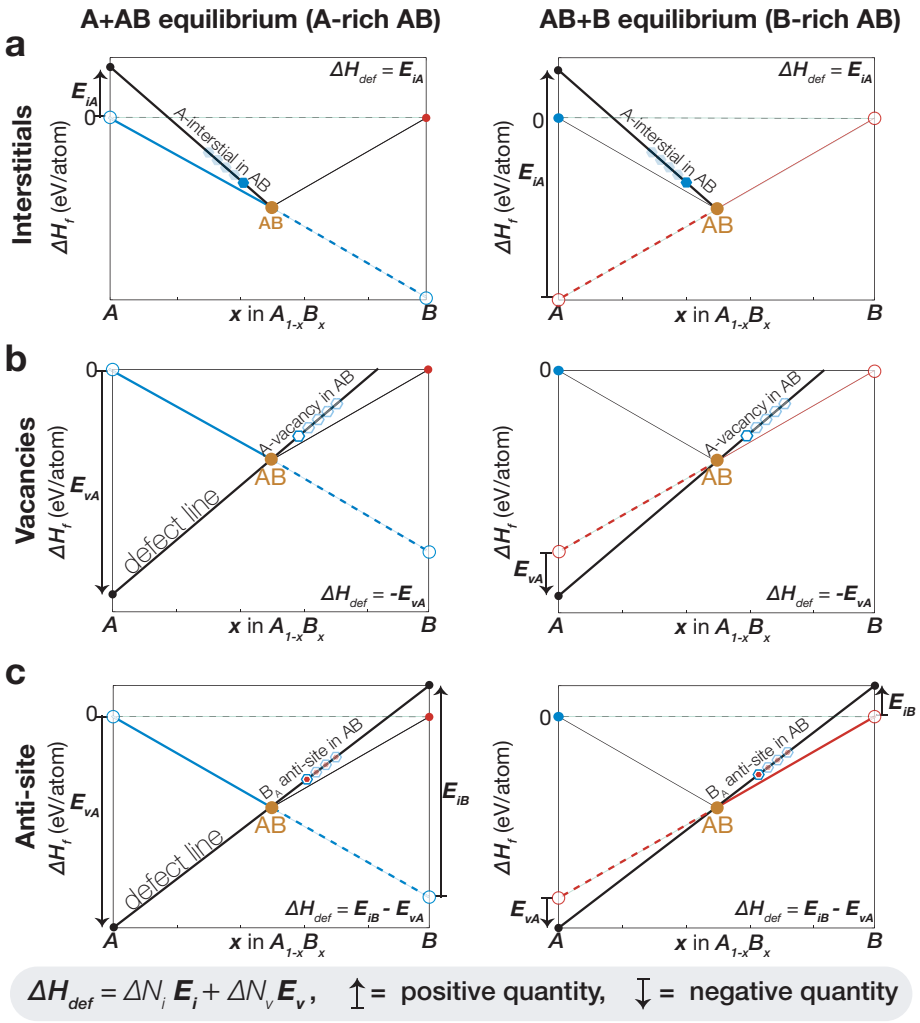

Figure 3: (a-c) Graphical solutions for defect energy ΔH_{def} of (a) A interstitial, (b) A vacancy, and (c) B_A antisite defects in the binary compound AB. Formation energy (ΔH_f) of the defect-free AB structure is given by the orange circle. ΔH_f of defective AB structures are shown as filled hexagons for interstitials (a), empty hexagons for vacancy defects (b), or a combination for anti-sites (c). Defective structures with the same value of ΔH_{def} are shown by translucent symbols and fall on the 'defect line' (solid black line). The left and right columns correspond to A-rich and B-rich equilibrium, respectively. The chemical potentials of A and B corresponding to these equilibrium conditions (large, empty circles) are determined from intercepts of the common tangent lines (blue and red lines in the left and right columns respectively). ΔH_{def} is determined using intercept (for example E_i) between the defect line and the common tangent line on the A and B-component axis. The sign of these quantities are are given by the direction of the arrows next to them (see grey box). The expression to calculate ΔH_{def} is given in each panel. The general expression for calculating ΔH_{def} for all defect types in is given in the grey box at the bottom where $\Delta N_i = 0$ or 1 and $\Delta N_v = 0$ or -1 depending on whether the number of atoms of a particular species is added (1), removed (-1) or unchanged (0) in the defect.

of the expression, all ΔH_f terms necessary to determine ΔH_{def} can be read directly from the convex-hull diagram (Figure 3). Full derivations for each defect type in the general cases of a model binary compound A_pB_q and a ternary compound $A_pB_qC_r$ are given in the Methods section.

Figure 3 shows example sketches of various simple point defect types (interstitials, vacancies and antisites) in the compound AB. The ΔH_f of the defective structures are drawn such that they lie above the convex-hull, signifying metastability at $T = 0K$. Note that, depending on how each defect type changes the stoichiometry of the compound, ΔH_f of the defective structures are either shown (Figure 3) at the percentage compositions $x < 0.5$ (A-interstitials) or $x > 0.5$ (A-vacancies, B_A anti-sites). Structures with larger defect concentrations lie further away from the x = 0.5 composition. We draw two columns for each panel in Figure 3 indicating the chemical potentials (see unfilled circles) in A-rich and B-rich equilibrium conditions.

To obtain ΔH_{def} graphically for the example of A-interstitials in Figure 3a, we simply join the ΔH_f of the pristine compound and the defective structure with a line. We will call this line as the "defect line" (see thick black line in Figure 3 a). We extend the defect line to find the energy where it meets the A-component axis (filled black circle at $x = 0$). We determine ΔH_{def} by simply subtracting the chosen chemical potential of A from this energy. Based on the geometry of the convex-Hull, we see that ΔH_{def} for A-rich equilibrium is smaller than the in the case of A-poor equilibrium, as one might expect. In the case of A-vacancies, we extend the defect line in the same way to find the energy where it meets the A-component axis. To determine the ΔH_{def} we again subtract the chosen chemical potential of A, but this time we change the sign by multiplying by a factor of -1.

Based on the examples of the vacancy and interstitial defects, we learn a couple of rules:

(i) for defects involving the atomic species i, we extend the defect line towards the i-component axis to find the energy of intersection

(ii) after subtracting the chosen chemical potential of the species i, we either multiply

by a factor of +1 or -1 depending on whether the atom was added to or removed from the structure to form the defect.

For the example of B_A anti-site defects, which is associated with both A and B atoms, we extend the defect line on either sides to intersect with the A and B-component axis. We determine the energy of intersection and subtract the corresponding choice of chemical potential. For the term on the A side, we treat it as a vacancy and multiply by a factor of -1. For the term on the B side, we treat it as an interstitial and multiply by a factor of 1. To obtain the ΔH_{def} we then add the two terms.

For the sake of our demonstration, we have drawn more defects at larger concentrations using translucent symbols in Figure 3. Since all these points fall on the same defect line they have the same value of ΔH_{def}, i.e same defect energy per-defect. On the scale of most convex-hull diagrams, the ΔH_f of the defective structures and the compound calculated from first-principles calculations can often seem to fall on a line (see Figure S2) suggesting a constant ΔH_{def}.[35,36] However, at compositions closer to the compound deviations from linearity are quite evident and evaluation of an accurate dilute limit ΔH_{def} requires checking for convergence with respect to defect concentrations.[37–39] The non-linearity in ΔH_f values of defective structures can arise from band-filling effects accompanying changes in E_F with increasing concentrations of donor or acceptor defects, changes in electrostatic potential in the vicinity of a charged defect and defect-defect interactions (electrostatic and strain field interactions between the two defects).[37–39] Typically, the dilute limit ΔH_{def} is obtained using the defective structures closest in composition to the compound (as represented by the opaque defect symbols in Figure 3).

The visualization scheme in Figure 3 can also be used relate ΔH_{def} to key thermodynamic parameters used in CALPHAD based thermodynamic models[40] for calculating the phase diagram. Using the compound energy formalism, CALPHAD based models[40] describe off-stoichiometry by assesing the stability of metastable structures known as end-members.[41] An example of an end-member for the compound AB, is the structure at the pure B composition

obtained by removing all A-atoms of the structure. The Gibbs free energy of this A-vacancy end-member is given by the notation ${}^{o}G_{Va:B}$. Since the visualization scheme shown in Figure 3 uses the formation enthalpy of the defective structures, ΔH_{def} can be related to the enthalpic contribution ${}^{o}H_{Va:B}$ to ${}^{o}G_{Va:B}$. For this, we first note that the $\Delta H_{f,Va:B}$ of the metastable end-member is obtained by intersection point of the defect line (determined by dilute limit A-vacancy calculations) with the y-axis at pure B composition. From this, we see that ${}^{o}H_{Va:B} = \Delta H_{f,Va:B} + H^{o}_{B}$, where H^{o}_{B} is the enthalpy of the the elemental phase B. For the compound AB discussed in Figure 3, we see that $\Delta H_{f,Va:B} = \Delta H^{B-rich}_{V_A}$ where $\Delta H^{B-rich}_{V_A}$ is the defect energy of the A-vacancy under B-rich conditions and so ${}^{o}H_{Va:B} = \Delta H^{B-rich}_{V_A} + H^{o}_{B}$. We would like to note here however that while $\Delta H^{B-rich}_{V_A}$ is calculated from intercepts at pure A composition, whereas $\Delta H_{f,Va:B}$ is calculated from the intercept on the pure B composition. Therefore, $\Delta H_{f,Va:B}$ and $\Delta H^{B-rich}_{V_A}$ are not necessarily equal for all compounds and are related to each other by the stoichiometry of the compound itself. Relations between ΔH_{def} of other defects and the corresponding end-member enthalpies can be determined similarly.

Our graphical solution scheme to determine ΔH_{def} can be easily extended to multi-component systems (ternary, quaternary, etc.) for interstitials (see Figure 4 a,b) and vacancies using a pseudobinary construction. Plotting ΔH_f along the 1-dimensional composition line for these defects will naturally include the pure defect element enabling easy visualization of ΔH_{def} in the same way as described above. Although, visualization of ΔH_{def} for anti-site defects is not as straight-forward, it can still be done using a similar ΔH_f plot along a 1-D composition line joining the defect-free and the defective structures (see Figure 4 c,d). We note that even for the more complicated case of ternary compounds, the visualization scheme for all defect types are represented in simple two-dimensional plots (see Figure 4 b,d). This feature is extendable to more complex multicomponent phase spaces as well.

We compare ΔH_{def} calculated using our visualization scheme to those determined using equation 5 (see Supplementary Figure S3) in our previous work[42] for interstitials in ternary half-Heusler systems ($Nb_{0.8}CoSb$, $Ta_{0.8}CoSb$ etc.). The equality in ΔH_{def} calculated using

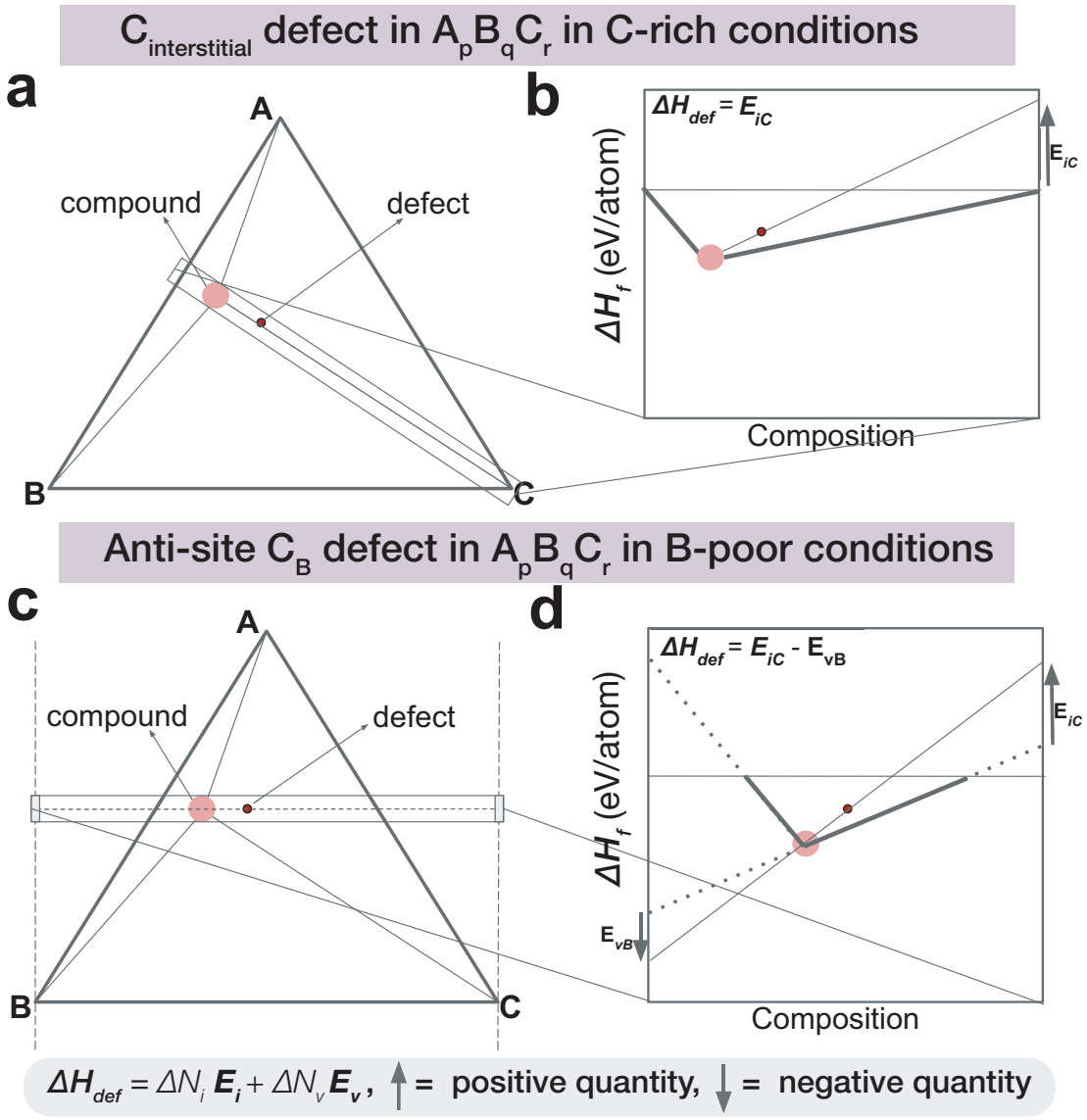

Figure 4: Graphical solution for defect energy (ΔH_{def}) of (a-b) C interstitial and (c-d) C_B anti-site defects in the ternary compound $A_pB_qC_r$. The compound and the defective structures are represented by large orange and small red circles respectively. Panels a and c show the ternary convex-hulls in which the compound $A_pB_qC_r$ is in equilibrium with elements A, B and C. Panels b and d show the ΔH_f-composition convex-hull along the 1-D composition slice containing both the defect and the compound. The ΔH_{def} are shown for (a-b) C-rich ($A_pB_qC_r$-C two-phase region) and (c-d) B-poor ($A_pB_qC_r$-A-C three-phase region) conditions. Similar to the case of binary compounds (see Figure 3) ΔH_{def} is determined using intercept between the common tangent line and the defect line. The expression to calculate ΔH_{def} is given in each panel. The general expression for calculating ΔH_{def} for all defect types in is given in the grey box at the bottom where $\Delta N_i = 0$ or 1 and $\Delta N_v = 0$ or -1 depending on whether the number of atoms of a particular species is added (1), removed (-1) or unchanged (0) in the defect.

the two methods serves as numerical proof to our derivations in the present work.

The visualization scheme presented in the current work is applicable for calculation of ΔH_{def} regardless of choice of chemical potential. The issue of multiple chemical potential values for calculating defect energetics of crystalline compounds is currently addressed using phase stability plots in chemical potential space.[3,43] The construction of these plots using a model binary convex-hull is described in the supplementary information (see Figure (S1)). While these plots can in principle be used to derive ΔH_{def} corresponding to various equilibria, chemical potential space in general tends to be quite abstract for visualization considering that stoichiometry of each phase involved is depicted by the slope of the lines. As a result, plotting in the chemical potential space is often used in relatively advanced thermodynamic analysis and are often left out of introductory materials science textbooks. Owing to its simplicity, the convex-hull based approach discussed here could be a suitable pedagogical tool for teaching defect thermodynamics to a broader audience.

Conclusion

In conclusion, we show that one can graphically solve for the defect formation energies (ΔH_{def}) of any multi-component compound within a two-dimensional convex-hull plot, including the effect of all possible chemical potentials. Using this visualization scheme, we integrate the thermodynamic analysis of phases and point defects within the same intuitive picture built in composition space. Considering that convex-hull diagrams are an introductory concept to a materials science audience and used widely today in predicting stability from high-throughput databases, our work can serve as a powerful tool to bring the understanding of defect thermodynamics to a larger audience.

Methods

Consider the model binary compound A_pB_q with $p+q$ atoms in its primitive cell. For the sake of simplicity, we assume that A_pB_q is the only compound in the binary system $A-B$. To re-write the expression for ΔH_{def} given in 5, we assume that the defect is being created in a supercell which is l times larger in volume than the primitive cell. Then the formation energies ($\Delta H_f^{pristine}$) of the pristine (defect-free) structure is given by

$$\Delta H_f^{pristine} = \frac{E_{pristine} - lp\,\mu_A - lq\,\mu_B}{l(p+q)} \tag{7}$$

where $E_{pristine}$ is the total energy of the pristine structure. Similarly, the formation energy on the defective structure ΔH_f^{defect} is given by

$$\Delta H_f^{defect} = \frac{E_{defect} - lp\,\mu_A - lq\,\mu_B - \Sigma\,\Delta N_i\mu_i}{l(p+q) + \Sigma\,\Delta N_i} \tag{8}$$

where E_{defect} is the total energy of the defective structure. For the sake of generality we will write the chemical potential of the atomic species i as

$$\mu_i = \mu_i^o + \Delta\,\mu_i \tag{9}$$

where μ_i^o is the chemical potential of the elemental phase and $\Delta\mu_i$ is the composition dependent change in chemical potential. We rearrange the equations 7 and 8 to write down their total energies $E_{pristine}$ and E_{defect} in terms of the formation energies (ΔH_f) of the structures. We then substitute these expressions in equation 5 and simplify to get a general expression for ΔH_{def}

$$\Delta H_{def} = (l(p+q) + \Sigma\,\Delta N_i)\left([\Delta H_f^{defect} - \Delta H_f^{pristine}] + \frac{(\Sigma\,\Delta N_i)\Delta H_f^{pristine}}{l(p+q) + \Sigma\,\Delta N_i}\right) - \Sigma\,\Delta N_i\Delta\mu_i \tag{10}$$

We will further simplify this expression for interstitials anti-sites and vacancies on a case-by-case basis

Frenkel and Schottky Defects

Consider the case of complex defects Schottky, Frenkel and anti-site swapping defects in which case the term $\Sigma\Delta N_i\Delta\mu_i$ in equation 10 is a constant $l(p+q)\ \Delta H_f^{pristine}$. Hence, following from equation 10 the expression for ΔH_{def} becomes independent of chemical potential and the defect energy for these complex defects takes a constant value.

Interstitial

Consider the case of A-interstitial defect in A_pB_q for which $\Delta N_A = 1$ and $\Delta N_B = 0$. For the sake of simplicity let us assume that that A_pB_q is in equilibrium with the the element A such that for $A-$rich conditions $\Delta\mu_A = 0$. So Equation 10 then becomes

$$\Delta H_{def} = (l(p+q)+1)\left([\Delta H_f^{defect} - \Delta H_f^{pristine}] + \frac{\Delta H_f^{pristine}}{l(p+q)+1}\right) \tag{11}$$

The factor $l(p+q)+1$ depends on the composition of the pristine and defective structures and can be written as this factor as

$$f_A^{interstitial} = (l(p+q)+1) = \frac{1 - x_A^{pristine}}{x_A^{defect} - x_A^{pristine}} \tag{12}$$

where x_i is the percentage (for component i) composition of a particular structure. We call this factor f_i^k as the "projection factor", where k describes the type of defect in question. So ΔH_{def} becomes

$$\Delta H_{def} = f_A^{interstitial}\left([\Delta H_{defect} - \Delta H_{pristine}] + \frac{\Delta H_{pristine}}{f_A^{interstitial}}\right) \tag{13}$$

The second term in the expression, to which the projection factor is multiplied is the

convex-hull distance (E_{CH}) of the defective structure. The convex-hull distance (see example in Figure 2 c) is the vertical energy distance of a point from the convex-hull. So the expression for ΔH_{def} can be written succinctly as

$$\Delta H_{def} = f_A^{interstitial} E_{CH}^{interstitial} \tag{14}$$

From the equation 12 and 14 it becomes clear that the factor $f_A^{interstitial}$ 'projects' the convex-hull distance on to the A-component axis. The example (p = q = 1) of such a graphical solution for ΔH_{def} is shown in 3 a. However, the generality of our derivation dictates that equation 14 holds true even any case with $p \neq q$.

The graphical solution for ΔH_{def} in A-poor conditions can be understood by going back to equation 5. The difference in ΔH_{def} between A-rich and A-poor equilibrium conditions is simply given by the change in chemical potential $\Delta\mu_A$ between the two chemical conditions. Graphically this is taken care of by choosing chemical potentials pertaining to the A-poor equilibrium (see figure 3 a). Note that equation 14 does not hold true only for A-poor chemical conditions. To define ΔH_{def} more generally regardless of chemical potentials, we replace $E_{CH}^{interstitial}$ with 'extended convex-hull distance' ($E_{eCH}^{interstitial}$). We define $E_{eCH}^{interstitial}$ as the vertical energy distance of the interstitial defective structure from the line drawn to determine the chemical potential on the convex-hull plot. So for the A-poor equilibrium $E_{eCH}^{interstitial}$ will be the energy distance of the interstitial defective structure from the common tangent to the AB-B phase equilibria. The subtle difference between E_{eCH} and E_{CH} is that E_{eCH} is chemical potential dependent, whereas E_{CH} is not. We now re-write equation 14 more generally as

$$\Delta H_{def} = f_A^{interstitial} E_{eCH}^{interstitial} \tag{15}$$

Vacancy

For the case of $A-$vacancy defect $\Delta N_A = -1$ and $\Delta N_B = 0$. For A-rich conditions (assuming $\Delta\mu_A = 0$) equation 10 then becomes

$$\Delta H_{def} = (l(p+q)-1)\left([\Delta H_f^{defect} - \Delta H_f^{pristine}] - \frac{\Delta H_f^{pristine}}{l(p+q)-1}\right) \tag{16}$$

In this expression the projection factor can be written as

$$f_A^{vacancy} = (l(p+q)-1) = -\frac{1 - x_A^{pristine}}{x_A^{defect} - x_A^{pristine}} \tag{17}$$

Notice the factor of -1 in front of the expression for $f_A^{vacancy}$ making it slightly different from $f_A^{interstitial}$. Graphically, this means that unlike $f_A^{interstitial}$, $f_A^{vacancy}$ will flip the sign of the quantity projected onto the A-component axis. The simplified expression for ΔH_{def} then becomes

$$\Delta H_{def} = f_A^{vacancy}\left([\Delta H_f^{defect} - \Delta H_f^{pristine}] - \frac{\Delta H_f^{pristine}}{f_A^{vacancy}}\right) \tag{18}$$

Similar to the case of interstitial, the second term is the E_{CH} of the vacancy defect structure ($E_{CH}^{interstitial}$) and ΔH_{def} becomes

$$\Delta H_{def} = f_A^{vacancy}\, E_{CH}^{vacancy} \tag{19}$$

For our ΔH_{def} derivation to hold regardless of choice of chemical potential we re-write the expression in terms of $E_{eCH}^{vacancy}$

$$\Delta H_{def} = f_A^{vacancy}\, E_{eCH}^{vacancy} \tag{20}$$

Anti-site

For the case of A_B anti-site defect $\Delta N_A = 1$ and $\Delta N_B = -1$. Assuming A-rich conditions we get $\Delta\mu_A = 0$ and $\Delta\mu_B = \frac{p+q}{q} H_{pristine}$. After substituting in equation 10 and simplifying the expression

$$\Delta H_{def} = lp \left([\Delta H_f^{defect} - \Delta H_f^{pristine}] + \frac{\Delta H_f^{pristine}}{lq} \right) + lq \left([\Delta H_f^{defect} - \Delta H_f^{pristine}] + \frac{\Delta H_f^{pristine}}{lq} \right) \quad (21)$$

we proceed to identify the relevant projection factors as follows

$$f_A^{interstitial} = lq = \frac{1 - x_A^{pristine}}{x_A^{defect} - x_A^{pristine}} \quad (22)$$

$$f_B^{vacancy} = lp = -\frac{1 - x_B^{pristine}}{x_B^{defect} - x_B^{pristine}} \quad (23)$$

Using these expressions for $f_A^{interstitial}$ and $f_B^{vacancy}$ we can re-write ΔH_{def} as

$$\Delta H_{def} = f_B^{vacancy} \left([\Delta H_f^{defect} - \Delta H_f^{pristine}] + \frac{\Delta H_f^{pristine}}{f_A^{interstitial}} \right) + f_A^{interstitial} \left([\Delta H_f^{defect} - \Delta H_f^{pristine}] + \frac{\Delta H_f^{pristine}}{f_A^{interstitial}} \right) \quad (24)$$

rewriting ΔH_{def} again in terms of convex-hull distance of defective structure ($E_{CH}^{anti-site}$) in question we get

$$\Delta H_{def} = f_B^{vacancy} E_{CH}^{anti-site} + f_A^{interstitial} E_{CH}^{anti-site} \quad (25)$$

The two terms in this expression can be obtained by projecting the convex-hull distance of the defective structure ($E_{CH}^{anti-site}$) on the B and A-component axis respectively. For our ΔH_{def} derivation to hold regardless of choice of chemical potential we re-write the expression in terms of $E_{eCH}^{anti-site}$

$$\Delta H_{def} = f_B^{vacancy}\, E_{eCH}^{anti-site} + f_A^{interstitial}\, E_{eCH}^{anti-site} \tag{26}$$

ΔH_{def} in its most general form regardless of defect type and thermodynamic conditions can be written as

$$\Delta H_{def} = \Delta N_i^{added} f_i^{interstitial}\, E_{eCH}^{defect} - \Delta N_j^{removed} f_j^{vacancy}\, E_{eCH}^{defect} \tag{27}$$

where ΔN is the number of atoms added or removed in the defect for the component i and j respectively. E_{eCH}^{defect} is the extended convex-hull distance of the defective structure. Equation 27 can be used to derive all the equations on the panels of the Figure 3 (see bottom of the Figure 3).

Interstitial defects in a ternary compound

For the case of interstitial C_i defects in the ternary compound $A_pB_qC_r$ (see figure 4) consider the C-rich chemical conditions (two-phase region $A_pB_qC_r$-C). In this case $\Delta N_C = 1$ and $\Delta\mu_C = 0$. Using the general expression in equation 10, ΔH_{def} can be written as

$$\Delta H_{def} = (l(p+q+r)+1)\left([\Delta H_{defect}^{f} - \Delta H_{pristine}^{f}] + \frac{\Delta H_{pristine}^{f}}{l(p+q+r)+1}\right) \tag{28}$$

this expression can further be written as

$$\Delta H_{def} = f_C^{interstitial}\, E_{eCH} \tag{29}$$

where $f_C^{interstitial}$ is the projection factor given by $f_C^{interstitial} = (l(p+q+r)+1)$

Vacancy defects in a ternary compound

For the case of $C-$vacancy defects in the ternary compound $A_pB_qC_r$ (see figure 4) consider the C-rich chemical conditions (two-phase region $A_pB_qC_r$-C). In this case $\Delta N_C = -1$ and $\Delta\mu_C = 0$. Using the general expression in equation 10, ΔH_{def} can be written as

$$\Delta H_{def} = (l(p+q+r)-1)\left([\Delta H^f_{defect} - \Delta H^f_{pristine}] + \frac{\Delta H^f_{pristine}}{l(p+q+r)-1}\right) \tag{30}$$

this expression can further be simplified as

$$\Delta H_{def} = f_C^{interstitial}\ E_{eCH} \tag{31}$$

Anti-site defects in a ternary compound

For the case of anti-site C_B defects in the ternary compound $A_pB_qC_r$ (see figure 4) consider the B-poor chemical conditions (three-phase region $A_pB_qC_r$-A-C). Using the general expression in equation 10, ΔH_{def} can be written as

$$\Delta H_{def} = l(p+q+r)\left([\Delta H^f_{defect} - \Delta H^f_{pristine}] + \frac{\Delta H^f_{pristine}}{lq}\right) \tag{32}$$

this expression can further be written as

$$\Delta H_{def} = l(p+q+r)\ E_{eCH} \tag{33}$$

This quantity can be visualized as a projection of the convex-hull distance of the defective structure as shown in the figure 4.

Author Contributions

S. A. conceptualized the project, performed the formal analysis and wrote the manuscript. G. J. S. supervised the manuscript writing process. All authors reviewed and edited the manuscript.

Acknowledgements

We acknowledge the support of award 70NANB19H005 from U.S. Department of Commerce, National Institute of Standards and Technology as part of the Center for Hierarchical Materials Design (CHiMaD). S.A, J.P.M and G.J.S acknowledge support from the National Science Foundation (DMREF-1729487).

Data Availability

Methods section contains the entire data required to reproduce results of the present work.

References

(1) Miller, S. A.; Dylla, M.; Anand, S.; Gordiz, K.; Snyder, G. J.; Toberer, E. S. *npj Computational Materials* **2018**, *4*, 1–8.

(2) Goyal, A.; Gorai, P.; Anand, S.; Toberer, E. S.; Snyder, G. J.; Stevanović, V. *Chemistry of Materials* **2020**,

(3) Male, J.; Agne, M. T.; Goyal, A.; Anand, S.; Witting, I. T.; Stevanović, V.; Snyder, G. J. *Materials Horizons* **2019**, *6*, 1444–1453.

(4) Ohno, S.; Imasato, K.; Anand, S.; Tamaki, H.; Kang, S. D.; Gorai, P.; Sato, H. K.; Toberer, E. S.; Kanno, T.; Snyder, G. J. *Joule* **2017**,

(5) Berche, A.; Noutack, M. T.; Doublet, M.-L.; Jund, P. *Materials Today Physics* **2020**, 100203.

(6) Anand, S.; Gurunathan, R.; Soldi, T.; Borgsmiller, L.; Orenstein, R.; Snyder, G. J. *Journal of Materials Chemistry C* **2020**,

(7) Anand, S.; Wood, M.; Xia, Y.; Wolverton, C.; Snyder, G. J. *Joule* **2019**, *3*, 1226–1238.

(8) Tan, G.; Hao, S.; Hanus, R. C.; Zhang, X.; Anand, S.; Bailey, T. P.; Rettie, A. J.; Su, X.; Uher, C.; Dravid, V. P.; Snyder, G. J.; Wolverton, C.; Kanatzidis, M. G. *ACS Energy Letters* **2018**, *3*, 705–712.

(9) Maier, J. *Solid State Ionics* **1987**, *23*, 59–67.

(10) Goff, J.; Hayes, W.; Hull, S.; Hutchings, M.; Clausen, K. N. *Physical Review B* **1999**, *59*, 14202.

(11) Fergus, J. W. *Journal of power sources* **2006**, *162*, 30–40.

(12) Koettgen, J.; Grieshammer, S.; Hein, P.; Grope, B. O.; Nakayama, M.; Martin, M. *Physical Chemistry Chemical Physics* **2018**, *20*, 14291–14321.

(13) Omar, S.; Wachsman, E. D.; Jones, J. L.; Nino, J. C. *Journal of the American Ceramic Society* **2009**, *92*, 2674–2681.

(14) Hong, L.; Li, L.; Chen-Wiegart, Y.-K.; Wang, J.; Xiang, K.; Gan, L.; Li, W.; Meng, F.; Wang, F.; Wang, J.; Chiang, Y.-M.; Jin, S.; Tang, M. *Nature communications* **2017**, *8*, 1–13.

(15) Kuganathan, N.; Kordatos, A.; Kelaidis, N.; Chroneos, A. *Scientific reports* **2019**, *9*, 1–8.

(16) Hong, L.; Yang, K.; Tang, M. *npj Computational Materials* **2019**, *5*, 1–9.

(17) Brandt, R. E.; Poindexter, J. R.; Gorai, P.; Kurchin, R. C.; Hoye, R. L.; Nienhaus, L.; Wilson, M. W.; Polizzotti, J. A.; Sereika, R.; Zaltauskas, R.; Lee, L. C.; MacManus-Driscoll, J. L.; Bawendi, M. G.; Stevanovi, V.; Buonassisi, T. *Chemistry of Materials* **2017**, *29*, 4667–4674.

(18) Wang, F.; Bai, S.; Tress, W.; Hagfeldt, A.; Gao, F. *npj Flexible Electronics* **2018**, *2*, 1–14.

(19) Tang, Y.; Li, X.; Martin, L. H.; Cuervo-Reyes, E.; Ivas, T.; Leinenbach, C.; Anand, S.; Peters, M.; Snyder, G. J.; Battaglia, C. *Energy & Environmental Science* **2018**,

(20) Xia, K.; Nan, P.; Tan, S.; Wang, Y.; Ge, B.; Zhang, W.; Anand, S.; Zhao, X.; Snyder, G. J.; Zhu, T. *Energy & Environmental Science* **2019**, *12*, 1568–1574.

(21) Mao, J.; Niedziela, J. L.; Wang, Y.; Xia, Y.; Ge, B.; Liu, Z.; Zhou, J.; Ren, Z.; Liu, W.; Chan, M. K.; Chen, G.; Delaire, O.; Zhang, Q.; Ren, Z. *Nano Energy* **2018**, *48*, 189–196.

(22) Xia, K.; Liu, Y.; Anand, S.; Snyder, G. J.; Xin, J.; Yu, J.; Zhao, X.; Zhu, T. *Advanced Functional Materials* **2018**, *28*, 1705845.

(23) Gopal, C. B.; van de Walle, A. *Physical Review B* **2012**, *86*, 134117.

(24) Lany, S. *The Journal of chemical physics* **2018**, *148*, 071101.

(25) Yamazaki, Y.; Babilo, P.; Haile, S. M. *Chemistry of Materials* **2008**, *20*, 6352–6357.

(26) Schmitt, R.; Nenning, A.; Kraynis, O.; Korobko, R.; Frenkel, A. I.; Lubomirsky, I.; Haile, S. M.; Rupp, J. L. *Chemical Society Reviews* **2020**, *49*, 554–592.

(27) Lany, S.; Zunger, A. *Physical Review Letters* **2007**, *98*, 045501.

(28) Saal, J. E.; Kirklin, S.; Aykol, M.; Meredig, B.; Wolverton, C. *Jom* **2013**, *65*, 1501–1509.

(29) Kirklin, S.; Saal, J. E.; Meredig, B.; Thompson, A.; Doak, J. W.; Aykol, M.; Rühl, S.; Wolverton, C. *npj Computational Materials* **2015**, *1*, 15010.

(30) Jain, A.; Ong, S. P.; Hautier, G.; Chen, W.; Richards, W. D.; Dacek, S.; Cholia, S.; Gunter, D.; Skinner, D.; Ceder, G.; Persson, K. A. *Apl Materials* **2013**, *1*, 011002.

(31) Curtarolo, S.; Setyawan, W.; Wang, S.; Xue, J.; Yang, K.; Taylor, R. H.; Nelson, L. J.; Hart, G. L.; Sanvito, S.; Buongiorno-Nardelli, M.; Mingo, N.; Levy, O. *Computational Materials Science* **2012**, *58*, 227–235.

(32) Tang, F.; Hallstedt, B. *Calphad* **2016**, *55*, 260–269.

(33) Lukas, H.; Fries, S. G.; Sundman, B. *Computational thermodynamics: the Calphad method*; Cambridge university press, 2007.

(34) Freysoldt, C.; Grabowski, B.; Hickel, T.; Neugebauer, J.; Kresse, G.; Janotti, A.; Van de Walle, C. G. *Reviews of modern physics* **2014**, *86*, 253.

(35) Pomrehn, G. S.; Toberer, E. S.; Snyder, G. J.; van de Walle, A. *Physical Review B* **2011**, *83*, 094106.

(36) Zeier, W. G.; Anand, S.; Huang, L.; He, R.; Zhang, H.; Ren, Z.; Wolverton, C.; Snyder, G. J. *Chemistry of Materials* **2017**, *29*, 1210–1217.

(37) Doak, J. W.; Michel, K. J.; Wolverton, C. *Journal of Materials Chemistry C* **2015**, *3*, 10630–10649.

(38) Lany, S.; Zunger, A. *Physical Review B* **2008**, *78*, 235104.

(39) Lany, S.; Zunger, A. *Modelling and simulation in materials science and engineering* **2009**, *17*, 084002.

(40) Liu, Z.-K. *Journal of phase equilibria and diffusion* **2009**, *30*, 517–534.

(41) Peters, M.; Doak, J. W.; Zhang, W.-W.; Saal, J.; Olson, G. B.; Voorhees, P. W. *Calphad* **2017**, *58*, 17–24.

(42) Anand, S.; Xia, K.; Zhu, T.; Wolverton, C.; Snyder, G. J. *Advanced Energy Materials* **2018**, *8*, 1801409.

(43) Miller, S. A.; Gorai, P.; Aydemir, U.; Mason, T. O.; Stevanović, V.; Toberer, E. S.; Snyder, G. J. *Journal of Materials Chemistry C* **2017**, *5*, 8854–8861.

(44) Goyal, A.; Gorai, P.; Peng, H.; Lany, S.; Stevanović, V. *Computational Materials Science* **2017**, *130*, 1–9.